Journal of Alloys and Compounds 919 (2022) 165773

Contents lists available at ScienceDirect

Journal of Alloys and Compounds

journal homepage: www.elsevier.com/locate/jalcom

Composition and property optimization of rare-earth-free Mn-Al-C magnet by phase stability and magnetic behavior analysis

Sumin Kim[a,1], Minyeong Choi[b,1], Hoyun Won[b], Hyun-Sook Lee[a], Wonchel Lee[b,d], Seong-Gon Kim[c], Wooyoung Lee[a,*], Yang-Ki Hong[b,*]

[a] Department of Materials Science and Engineering, Yonsei University, 50 Yonsei-ro, Seodaemun-gu, 03722 Seoul, Republic of Korea
[b] Department of Electrical and Computer Engineering, The University of Alabama, Tuscaloosa, AL 35487, USA
[c] Department of Physics and Astronomy and Center for Computational Sciences, Mississippi State University, Mississippi State, MI 39792, USA
[d] Samsung Electro-Mechanics Co. Ltd., Suwon 16674, Republic of Korea

ARTICLE INFO

Article history:
Received 8 February 2021
Received in revised form 11 January 2022
Accepted 4 June 2022
Available online 6 June 2022

Keywords:
Permanent magnets
Carbon-doped MnAl
Phase stability
Electronic structure
Magnetic properties

ABSTRACT

Mn-Al-C system offers a possibility of rare-earth-free permanent magnets with the reduced temperature-dependent deterioration of magnetic properties. The Mn-Al-C alloy composition and magnetic properties have been optimized via calculations of electronic structures and phase stability of $L1_0$-ordered ferromagnetic τ-phase $(Mn_{0.5}Al_{0.5})_{100-x}C_x$. The WIEN2k program package, Vienna Ab-initio simulation package (VASP), and Alloy Theoretic Automated Toolkit (ATAT) were used to calculate and identify the optimal carbon content for the most stable τ-phase of the $L1_0$-structured Mn-Al-C. We used the Brillouin function and Callen-Callen semiempirical relation to obtain the saturation magnetization and magnetocrystalline anisotropy constant at elevated temperatures. It was found that a carbon content of 2.33 at% gives the most stable τ-phase $L1_0$ $(Mn_{0.5}Al_{0.5})_{100-x}C_x$ that has the lowest formation energy and highest saturation magnetization among the studied carbon contents (x = 0–3.03 *at%*). The magnetocrystalline anisotropy constant at 0 K increases with increasing the carbon content. Therefore, the carbon-doped Mn-Al becomes magnetically harder than the pure $Mn_{50}Al_{50}$. However, the anisotropy constant decreases at 300 K as the carbon content increases. The Curie temperature decreases to 590 K at x = 2.33 from 685 K at x = 0.0. The estimated saturation magnetization was approximately 130 emu/g at 300 K, leading to 18 MGOe under $B_s = B_r$ and $H_{ci} > B_r/2$. Therefo$_r$e, it is highly probable that Mn-Al-C potentially fills the gap between 10 and 30 MGOe magnets. The results in this study quantify and explain the reason for widely studying the approximately 2 at% carbon-doped Mn-Al systems.

1. Introduction

The application of permanent magnets (PMs) has been expanding towards sustainable energy devices, including electric vehicle (EV) motors, wind power generators, and flying car (drone) motors. The figure of merit for a PM is the maximum energy product, $(BH)_{max}$, in the unit of MGOe. The $(BH)_{max}$ can be estimated as $(BH)_{max} = (B_r)^2/4$ for $H_{ci} > B_r/2$ or $(BH)_{max} = (B_r - H_{ci})H_{ci}$ for $H_{ci} < B_r/2$, assuming an ideal rectangular hysteresis loop [1,2]. B_r is the remanent magnetization and H_{ci} is the coercivity of the magnetic material. The torque of the motor and power densities are determined by $(BH)_{max}$. Therefore, a high magnetization and coercivity, high Curie temperature (T_c), and high magnetocrystalline anisotropy constant (K) are required.

There is a sizeable permanent magnet market for the range 10–30 MGOe; however, no permanent magnet has $(BH)_{max}$ between 10 MGOe (Alnico/Ferrite) and 30 MGOe (Sm-Co or Nd-Fe-B). Rare-earth-free magnetic materials, such as MnBi, MnAl, and MnGa, potentially fill the gap between Alnico/Ferrite and Sm-Co or Nd-Fe-B [1]. In particular, the $L1_0$ τ-phase MnAl has attracted considerable attention because of its high magnetic moment, high magnetocrystalline anisotropy constant, high Curie temperature (650 K), and low density (5.3 g/cm^3) [1–7]. Most recently, MnBi-Sn displayed 14.3 MGOe of $(BH)_{max}$ at 300 K [8], which is close to the theoretical 17.7 MGOe of *LTP* MnBi [8,9].

* Corresponding authors.
E-mail addresses: wooyoung@yonsei.ac.kr (W. Lee), ykhong@eng.ua.edu (Y.-K. Hong).
[1] Co-first author.

https://doi.org/10.1016/j.jallcom.2022.165773
0925-8388/

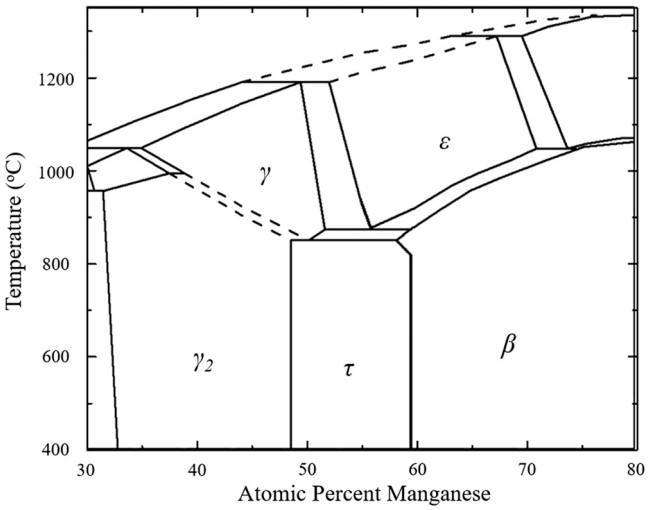

Fig. 1. Partial Mn–Al binary phase diagram [5].

The theoretical upper limit of $(BH)_{max}$ for the $L1_0$ τ-phase MnAl is 14 MGOe [10,11]; it is 12.64 MGOe for $L1_0$ τ-phase $Mn_{50}Al_{50}$, under the assumption $B_r = 0.7B_s$ [6]. Furthermore, Cui et al. have reported that the theoretical upper limits of $(BH)_{max}$ for the Mn-Al and Mn-Al-C alloys are 13.2 MGOe and 16.8 MGOe, respectively [12]. The comprehensive review results of rare-earth-free permanent magnets, including Mn-Al, are well documented in Ref. [12].

The highest experimental $(BH)_{max}$ is 7 MGOe for $L1_0$ τ-phase Mn-Al-C [13]. This $(BH)_{max}$ is still very small compared to the theoretical upper limit because of the narrow range of the $L1_0$ τ-phase in the phase diagram shown in Fig. 1, indicating a phase-stability issue. This implicates some difficulty of obtaining τ-phase and high coercivity. Fig. 2 represents two types of transformations occurring during the synthesis process. One is the crystallographic transformation, that is, $\varepsilon \rightarrow \varepsilon' \rightarrow \tau$, and the other is the magnetic transformation, that is, A3 (anti-ferromagnetic) → B19 (intermediate ferromagnetic) → metastable $L1_0$ (ferromagnetic). The $L1_0$ τ-phase MnAl forms within a narrow composition range of 48–59 at% (65.3–74.6 wt%) of Mn, as shown in Fig. 2 [3–5].

$L1_0$ τ-phase Mn-Al is conventionally synthesized by rapidly quenching the high-temperature ε-phase Mn-Al to room temperature, then annealing at temperatures between 350 and 650 °C [14,15]. Tong et al. have reported a saturation magnetization (σ_s) of 125 emu/g and coercivity (H_{ci}) of 2.04 KOe for $Mn_{54}Al_{46}$ [16], and a σ_s of 118 emu/g is reported for $Mn_{55}Al_{45}$ [17]. The prolonged annealing at elevated temperatures results in the transformation or decomposition of the τ-phase Mn-Al phase to the stable and nonmagnetic cubic β-Mn and trigonal γ_2-Al_8Mn_5 phases [3,18]. This decomposition is because of the nature of the metastable τ-phase Mn-Al phase. Therefore, it is challenging to obtain a high purity, equiatomic $L1_0$ τ-phase $Mn_{50}Al_{50}$ experimentally.

To improve the stability of the $L1_0$ τ-phase Mn-Al phase, Mn-Al is doped with a small amount of carbon. Otani et al. reported that the solubility limit of carbon to 72 wt% Mn-Al is 0.6 wt% (2.10 at%), and the excess of carbon effectively increases the coercivity because of the presence of the Mn_3AlC precipitates [13]. The carbon atom is located at (½, ½, ½) in the $L1_0$ Mn-Al unit cell. The stability of metastable τ-phase Mn-Al is improved by adding a C atom [19]. The most studied carbon-doped composition is Mn > 54 at% because of the less probability of occurrence of the secondary phases in the Mn-Al alloy. Nguyen et al. reported 570 kA/m (111.8 emu/g) of σ_s for mechanically alloyed $Mn_{54.2}Al_{43.8}C_2$ [20], and Fang et al. have obtained 117 emu/g of σ_s and estimated 137 emu/g for the theoretical maximum magnetization of drop-cryo-milled $Mn_{55}Al_{45}C_2$ [21]. Furthermore, the $Mn_{55}Al_{43}C_2$ alloy was fabricated by the high-pressure torsion deformation process. Its coercivity and σ_s were 2.4 kOe and 115 emu/g, respectively [22]. The most studied Mn-Al-C system is based on approximately 2 at% of the carbon content to stabilize the τ-phase, thereby obtaining a high saturation magnetization.

The equiatomic alloy 50 at% MnAl has been rarely studied because the τ-phase Mn-Al forms within a narrow composition range from 48 to 59 at%, but with Mn-rich compositions (Mn > 54 at%). It is worth noting that two stable paramagnetic phases exist near the τ-phase region in Fig. 1: nonmagnetic cubic β-Mn for Mn-rich composition and trigonal γ_2-Al_8Mn_5 for Al-rich composition. These two phases degrade the magnetic properties of $L1_0$ τ-phase Mn-Al.

Sakuma performed first-principles calculations on $L1_0$ τ-phase $Mn_{50}Al_{50}$ and found that the magnetocrystalline anisotropy energy (H_k) is dependent on the c/a ratio [7]. Pasko et al. synthesized Mn-Al with various compositions, such as $Mn_{50}Al_{50}$, $Mn_{49}Al_{49}C_2$, $Mn_{55}Al_{45}$,

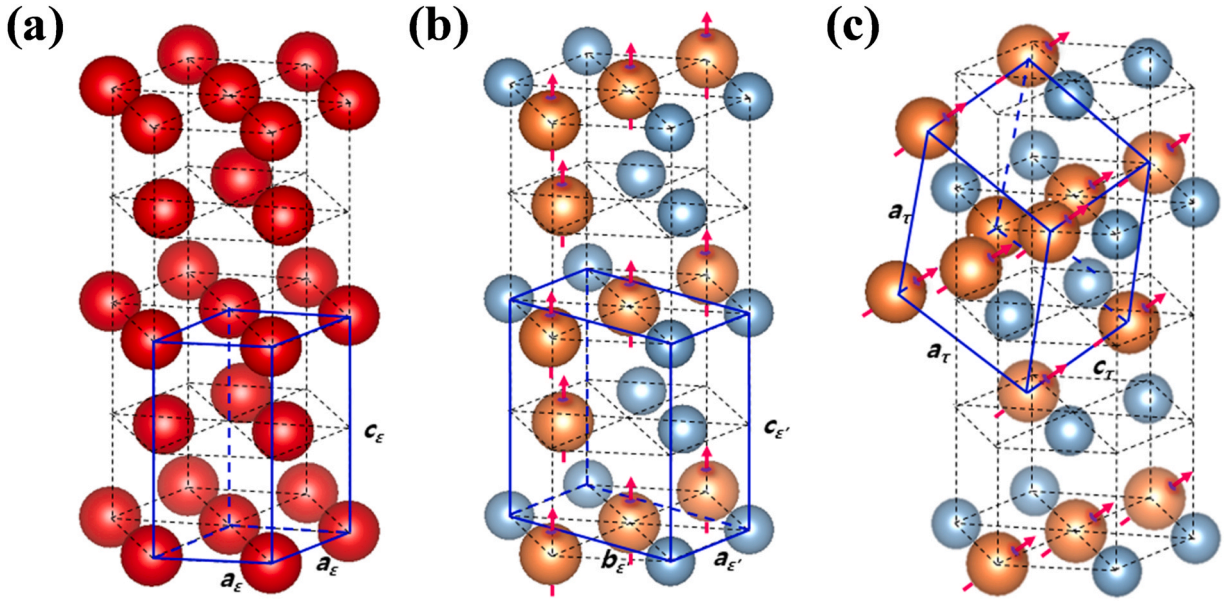

Fig. 2. Crystallography of (a) A3 (ε phase), (b) B19 (ε′ phase) and (c) $L1_0$ tetragonal (τ phase) for MnAl (red: Mn or Al, orange: Mn, blue: Al).

and $Mn_{54}Al_{44}C_2$ alloys, and characterized them for their magnetic properties [23]. $Mn_{54}Al_{44}C_2$ shows the highest saturation magnetization among the studied compositions. It holds a Curie temperature of 610 K. An atomistic spin dynamics model for the ideal τ-phase $Mn_{50}Al_{50}$ was developed using first-principles calculations [24]. Cuo et al. have reported a σ_s of approximately 390 emu/cm^3 (73.6 or 76.5 emu/g) and a coercivity (H_{ci}) of 2.2 kOe for the $Mn_{50}Al_{50}$/Al bilayer film after annealing the film at 673 K for 30 min [25]. These experimental results indicate that alloying Mn-Al with carbon establishes the τ-phase stability. Carbon plays a crucial role in improving magnetization and coercivity by suppressing the decomposition of the τ-phase into β-Mn and γ_2-Al_8Mn_5 phases. However, a theoretical understanding or prediction of the effect of carbon on the τ-phase stability, magnetocrystalline anisotropy, and magnetic moment at elevated temperatures remains unreported. The $Mn_{50}Al_{50}$ composition at the edge of the phase diagram, that is, paramagnetic γ_2 (Fig. 1) and the τ-phase are more stable in $Mn_{54}Al_{46}$; however, we chose the equiatomic $Mn_{50}Al_{50}$ composition to study the phase stability of Mn-Al-C and save computation energy.

The contribution of this study is threefold: the electronic structure calculation of Mn-Al-C, calculation of phase stability, and synthesis of τ-phase Mn-Al-C according to the theoretically identified composition. Furthermore, we also report the theoretical temperature dependence of magnetization M(T), magnetocrystalline anisotropy constant K(T), and composition dependence of Curie temperature T_c(x) of $(Mn_{0.5}Al_{0.5})_{100-x}C_x$. Determining the critical carbon content, which primarily stabilizes the τ-phase of $(Mn_{0.5}Al_{0.5})_{100-x}C_x$, and the experimental verification of the theoretically optimized carbon content is the focus of this study.

2. Methods

2.1. Computational

The crystal structures shown in Fig. 3 were used to calculate the electronic structures of $(Mn_{0.5}Al_{0.5})_{100-x}C_x$ (x = 0, 1.54, 2.33, and 3.03). The WIEN2k program package was used to calculate the electron density within an $L1_0$ τ-phase MnAl unit cell. We also used the Vienna Ab-initio simulation package (VASP), based on the density functional theory (DFT), to perform first-principles calculations under the collinear magnetic spin arrangement assumption. The density of states (DOS) and magnetocrystalline anisotropy energy (MAE) were then obtained. All spin-polarized and spin-orbit couplings are calculated by DFT within the generalized gradient approximation (GGA) [26], with a k-point of 8 × 8 × 8 and plane-wave cutoff energy of 350 eV. A frozen-core full-potential projected augmented wave (PAW) method was used to perform the first-principles calculations [27,28].

To calculate the electron density distribution ρ_r in $L1_0$ τ-phase $Mn_{50}Al_{50}$, we employed the WIEN2k package [29]. The partial atomic wave (as) in the atoms and the plane wave (ir) in the interstitial region are considered. The electron density ρ_{as} and ρ_{ir} are calculated by orthogonalizing the wave function Ψ(r). After combining ρ_{as} and ρ_{ir}, we obtain the total electron density ρ_r and construct the electron density map. The electron density map identifies the sites available in the Mn-Al unit cells for doping carbon atoms.

We use the Alloy Theoretic Automated Toolkit (ATAT: a collection of alloy theory tools) [30,31] to calculate the phase stability of $(Mn_{0.5}Al_{0.5})_{100-x}C_x$ (x = 0, 1.54, 2.33, 5.88, 11.11, and 20). The cluster expansion method parameterizes the physical properties of a multicomponent system depending on the atomic configuration [32]; therefore, the formation energy is calculated. As implemented in the ATAT, the MIT ab initio Phase Stability code [33] is used to construct the cluster expansion in conjunction with a first-principles code, that is, VASP. First-principles calculations obtain the relaxed lattice parameters and six total energies for six different compositions of Mn-Al-C. These values are used to calculate the effective cluster interactions (ECIs). The formation energy of the known structure $(Mn_{50}Al_{50})_{100-x}C_x$ is then calculated in terms of chemical composition. The lattice geometry finds the best structure for the phase stability of the Mn-Al–C system. The total energy determines the best cluster expansion for the Mn-Al-C structure through first-principles calculations (i.e., VASP). In cluster expansion formalism, $E(\sigma_1, \cdots\sigma_n) = \sum_\alpha J_\alpha \sigma_\alpha$, where E is the energy per atom of an alloy, J is the expansion coefficient, σ is the occupation variable, and α is a cluster. ECIs and the formation energy are presented for the underlying crystal structure.

The solution to the Kohn-Sham equation gives the DOS and MAE. First-principles calculations were performed using the VASP package based on DFT and a frozen-core full-potential PAW. The DFT within GGA is used to calculate all spin-polarized and spin-orbit couplings; therefore, Eigenvalue and Eigenfunction are obtained. The following valence electrons are used for the electronic structure calculations: $3d^5\ 4s^2$ for Mn, $3s^2\ 3p^1$ for Al, and $2s^2\ 2p^2$ for C. Accordingly, DOS ($\bar{n}$) is obtained by the difference of the integrated DOS (N) between two pins (i.e., the energy difference between two grid points) [34]. The saturation magnetization at 0 K (σ_s(0)) is then obtained from DOS. The MAE is calculated by the energy difference between the hard and easy spin directions. The calculated MAE is converted to the magnetocrystalline anisotropy constant K_u(0) as follows:

$$\Delta E_{MCA} = \sum_i \varepsilon_i(\hat{n}_1) - \sum_i \varepsilon_i(\hat{n}_2) = E^{total}(\hat{n}_1) - E^{total}(\hat{n}_2). \quad (1)$$

To estimate the magnetization at elevated temperatures, the Curie temperature (T_C) is calculated using the following mean-field approximation (MFA) expression [35]:

$$T_c = \frac{2}{3k_B} J_0 \gamma, \quad J_0 = \sum_j J_{0j} \quad (2)$$

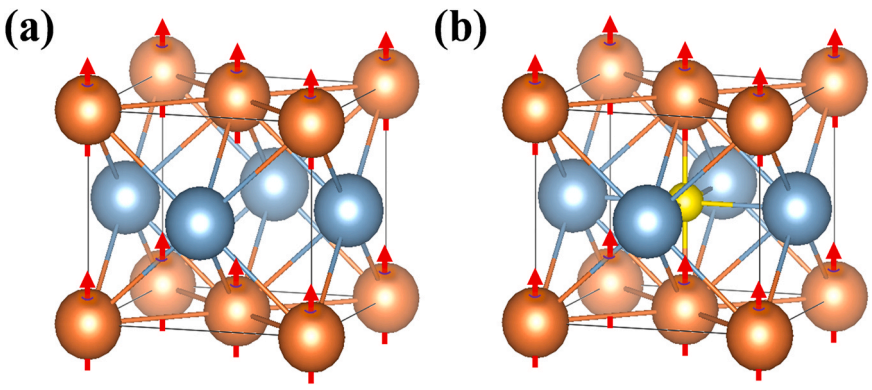

Fig. 3. (a) Magnetic structure of MnAl and (b) Mn-Al-C (orange: Mn, blue: Al, yellow: C).

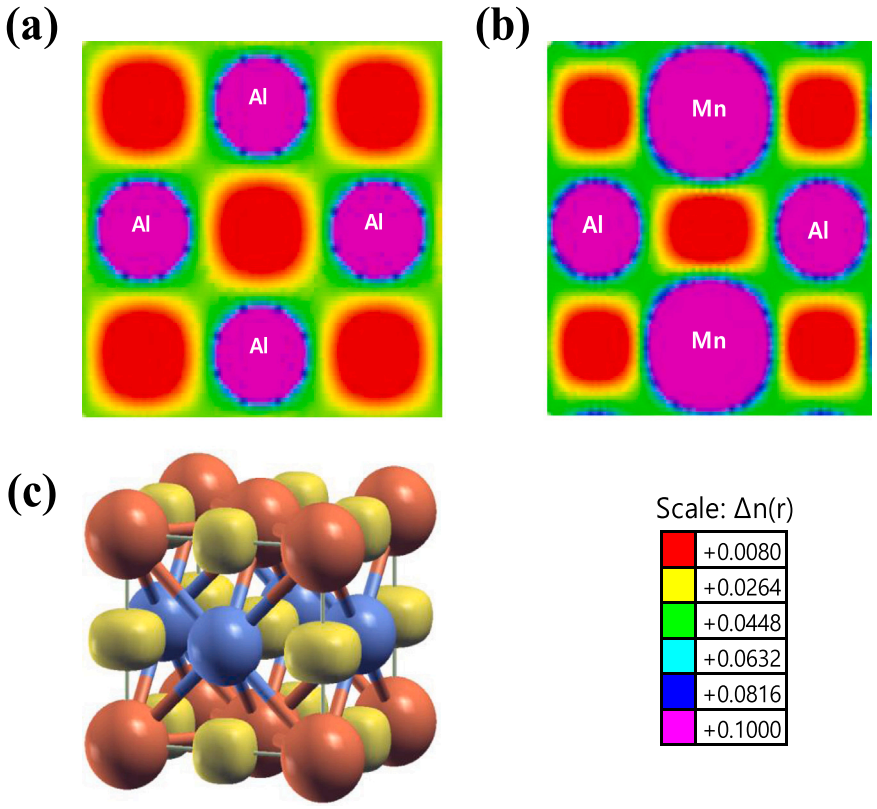

Fig. 4. 2D electron density map for (a) (0 0 ½) plane and (b) (0 ½ 0) plane and (c) 3D electron density map (yellow region: lowest electron density).

where k_B is the Boltzmann constant, J_0 is the molecular field parameter, and J_{0j} is the exchange integral. γ is obtained from $S(S+1)/S^2$ for the quantum spins and 1 for the classical spins. The exchange integral (J_{ij}) is obtained using the number of nearest neighbors (z_{ij}) and its corresponding distance (r_{ij}), that is, $J_{ij} = (\Delta_{ij} - \Delta_i - \Delta_j)/(4S_iS_jn_iz_{ij})$. $S_{i,j}$ is the quantum spin of the ith or jth Mn atom, $\Delta_{i,j}$ is the exchange energy difference between the ground and excited states with the ith or jth Mn atom, n_i is the number of ith atoms, and z_{ij} is the neighboring ith to the jth atom. The exchange integrals (J_{0j}) consider interactions over all the neighboring spins.

The temperature-dependent σ_s(T) ane K_u(T) are described by Eqs. (3) and (4), respectively. Accordingly, $\sigma_s(0)$, $K_u(0)$, and T_c are used in the calculation of σ_s(T) and K_u(T). $(BH)_{max}$(T) is then estimated at elevated temperatures. The Brillouin function ($B(J, a')$) can express the σ_s(T) curve [9]:

$$\sigma_s(T) = \sigma_s(0)\left(\frac{2J+1}{2J}coth\left(\frac{2J+1}{2J}a'\right) - \frac{1}{2J}coth\left(\frac{a'}{2J}\right)\right) = \sigma_s(0)B(J, a'), \quad (3)$$

where $a' = \frac{\sigma/\sigma_0}{T/T_c}\left(\frac{3J}{J+1}\right)$ and J is the angular quantum number.

Regarding K_u(T), the spin and orbital moments are calculated for magnetization along the hard and easy directions to obtain the magnetocrystalline anisotropy energy (MAE: E_{MAE}). The total energies calculated for these two directions are used to obtain the E_{MAE} and K_u (= E_{MAE}/unit-cell). Accordingly, $E_{MAE} = E_{<hard>} - E_{<easy>}$, where $E_{<hard>}$ is the energy with spin along the < 100 > direction and $E_{<easy>}$ is the energy with spin along the < 001 > direction. The temperature-dependent magnetocrystalline anisotropy constant is given by Eq. (4) [36]:

$$K_u(T) \propto K_u(0)\left(\frac{\sigma_s(T)}{\sigma_s(0)}\right)^{n(n+1)}, \quad (4)$$

where n is the power of the anisotropy function.

2.2. Experimental

$(Mn_{0.5}Al_{0.5})_{100-x}C_x$ (x = 0, 1.54, 2.33, and 3.03) powders were prepared by induction melting, heat treatment, melt-spinning, annealing, grinding, post-heat treatment, and magnetic separation. Commercial raw elements Mn (99.99 %), Al (99.99 %), and C (99.95 %) were mixed in the desired atomic ratios. Because Mn is rapidly oxidized in air, the Mn chips were cleaned in an aqueous solution of nitric acid immediately before use. Owing to the high vapor pressure of Mn, an excess of Mn (3 wt%) was added.

Furthermore, because of the significant difference in the melting temperature of each element, it is difficult to obtain a compositionally homogeneous Mn-Al-C alloy [37], and the C powder remained at the bottom of the alloy during the melting process. A mixture of Mn, Al, and C was heated at 1000 °C for 10 h in vacuum and cooled to room temperature. The resulting alloy ingot was melted and ejected onto the surface of a rotating copper wheel in a ribbon form under an Ar atmosphere at 50 kPa; the tangential speed of the wheel was set to 20 m/s. To obtain the ferromagnetic τ–phase of $(Mn_{0.5}Al_{0.5})_{100-x}C_x$, the melt-spun Mn-Al-C ribbons were annealed at an optimized temperature of 550 °C for 60 min in vacuum. The annealed ribbons were mechanically crushed into powder under an argon atmosphere using a SPEX 8000D high-energy shaker ball mill. Hardened steel bearing balls of 10 mm diameter were used as the milling medium. The ball-to-powder weight ratio was fixed at approximately 10:1. To prevent the heating of the vial and load, the milling process was performed for 10 min. The loading and sealing of the vials were performed with oleic acid in an Ar-controlled glove box. In general, the mechanical milling into powders can create the decomposition of τ–phase to equilibrium β and γ_2 phases [38–40]. Thereafter, the milled powders were heated again in vacuum for 15 min at 500 °C, which is the formation temperature of τ–phase [38–40]. Subsequently, magnetic separation, which was suggested in our previous

study [41], was performed to increase the ferromagnetic phase content.

The as-spun ribbons, annealed ribbons, and magnetically separated powders were characterized by X-ray diffraction (XRD, Bruker D8 Advance with LynxEye) with Cu Kα radiation to determine their phases. The morphology of the resultant powder was investigated by scanning electron microscopy (SEM, JEOL, JSM-7800F). The magnetic properties were measured at room temperature by vibrating sample magnetometry (VSM, Lakeshore 7410 series) under a maximum applied field of 30 kOe.

3. Results and discussion

We calculated the electron density of $L1_0$ τ-phase $Mn_{50}Al_{50}$ in Fig. 3(a) to confirm the availability of the interstitial sites in the $L1_0$ $Mn_{50}Al_{50}$ unit cell for carbon atoms. Fig. 4 illustrates an electron density map and confirms the available sites on the (0 0 ½) and (0 ½ 0) planes, as highlighted by red. The red regions are the most electron-deficient in the $Mn_{50}Al_{50}$ unit cell. These results are in good agreement with the previously reported results [42]. We inserted a carbon atom into the interstitial site, as shown in Fig. 3(b), and calculated the relaxed lattice constants for $(Mn_{0.5}Al_{0.5})_{100-x}C_x$. The relaxed lattice constants, volume, and c/a ratio are summarized in Table 1. All the lattice constants, a, b, c, and the unit cell volume increase as the carbon content increases from x = 0–3.03. An increase in the volume indicates that the carbon atoms occupy the interstitial sites (½, ½, ½). Moreover, the c/a ratio gradually increases for x > 0.

The relaxed lattice constants were used in the phase stability calculation of $(Mn_{0.5}Al_{0.5})_{100-x}C_x$ (x = 0–20). We used the ATAT tool kits to calculate the phase stability, identifying the most τ-phase-stable composition among the studied compositions. The kits are based on the MIT ab initio Phase Stability code, described in Sections 2-1. Fig. 5 shows the composition-dependent formation energy ($0 \le x \le 20$) and a convex-hull-like curve, along with the experimental magnetization for $(Mn_{0.5}Al_{0.5})_{100-x}C_x$ ($0 \le x \le 3.03$). These are the results of ATAT performance and VSM characterization. Negative formation energy relative to pure $Mn_{50}Al_{50}$ was obtained for the compositions ($0 \le x \le 20$). The composition with x = 2.33 shows the lowest formation energy, i.e., the ground-state energy, and the highest experimental magnetization. This demonstrates that the $L1_0$ τ-phase $(Mn_{0.5}Al_{0.5})_{100-x}C_x$ is mostly stable at x = 2.33 among the studied compositions, explaining well the reason for widely studying the approximately 2 at% carbon-doped Mn-Al.

We used the relaxed lattice constants to calculate the electronic structure of $L1_0$ τ-phase $(Mn_{0.5}Al_{0.5})_{100-x}C_x$. The calculation results, i.e., DOS and partial spin resolved DOS (pDOS), are shown in Fig. 6. Fig. 6(a) is the DOS for the undoped $L1_0$ τ-phase Mn-Al (x = 0), (b) is the DOS for x = 1.54, (c) is the DOS for x = 2.33, and (d) is the DOS for x = 3.03. The pDOS are shown in Fig. 6(e–h): (e) x = 0, (f) x = 1.54, (g) x = 2.33, and (h) x = 3.03. The Fermi energy resides in the deep valleys in both majority and minority bands, suggesting the electronic structure stability in $Mn_{50}Al_{50}$. The doping of $L1_0$ τ-phase Mn-Al with carbon significantly changes DOS. A strong DOS peak appears near − 11 eV in the $L1_0$ τ-phase Mn-Al-C (x = 2.33), implying a change in the electronic structure. The valence band splits into two bands. The

Table 1
Relaxed lattice constant for $(Mn_{50}Al_{50})_{100-x}C_x$.

x (*at*%)	Lattice Constant, *u.c.* (Å)			Volume, *u.c.* (Å^3)	*c*/*a*
	a	*b*	*c*		
0	3.84	3.84	3.34	49.26	0.870
0.78	3.85	3.85	3.38	50.10	0.878
1.54	3.89	3.89	3.42	51.75	0.879
2.33	3.92	3.92	3.45	53.01	0.880
3.03	3.94	3.94	3.47	53.87	0.881

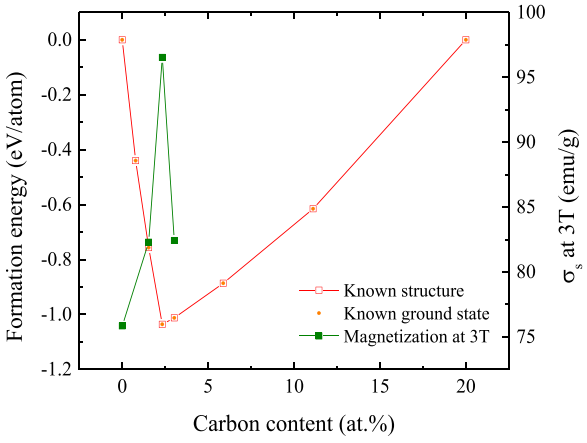

Fig. 5. Formation energy and experimental magnetization of $(Mn_{0.5}Al_{0.5})_{100-x}C_x$.

lower band starts at approximately − 11 eV and ends at approximately − 8.5 eV. This lower band is primarily attributed to the carbon s-state. The upper band starts at − 8.5 eV and occupies up to the Fermi level. Electrons from Mn primarily contribute to this upper band. No gap appeared between the valence and conduction bands; therefore, the $L1_0$ τ-phase Mn-Al is metallic. The magnetic moment (μ_B/unit cell) was obtained from the DOS in Fig. 6 and converted to the $\sigma_s(0)$ in the unit of emu/g.

We calculated $E_{MAE}(0)$ and $K_u(0)$ (= E_{MAE}/unit-cell) of $(Mn_{0.55}Al_{0.45})_{100}C_2$ using the method presented in Section 2.1. Table 2 summarizes the $\sigma_s(0)$ and $K_u(0)$. The $\sigma_s(0)$ decreases from 143 emu/g to 137 emu/g as the carbon content increases from x = 0 to x = 3.03. Notably, the $\sigma_s(0)$ is138 emu/g at x = 2.33. The K_u at 0 K increases to 1.45 MJ/m^3 at x = 3.03 from 1.37 MJ/m^3 at x = 0, which is in good agreement with the Ref. [7]. Therefore, the carbon-doped $L1_0$ τ-phase Mn-Al-C became magnetically harder than $L1_0$ τ-phase $Mn_{50}Al_{50}$ (x = 0). However, the decrease in the $\sigma_s(0)$ is insignificant. Fang et al. reported a σ_s of 117 emu/g for $(Mn_{0.55}Al_{0.45})_{100}C_2$ at 300 K [21], which is smaller than $\sigma_s(0)$. The calculated magnetization and magnetocrystalline anisotropy constant at 300 K will be discussed and compared with the experimental results.

To estimate σ_s(300 K), and K_u(300 K), we have calculated the Curie temperature (T_C) of $(Mn_{0.5}Al_{0.5})_{100-x}C_x$ (x = 0–3.03) using the method described in Sections 2-1. The T_C and room-temperature σ_s and K_u are summarized in Table 3. The calculated T_C, σ_s(0 K), and K_u (0 K) were used in the calculation of σ_s(T) and K_u(T) according to Eqs. (3) and (4). Fig. 7 shows the calculated T_C with carbon content (x) and experimental T_C [13,43]. The T_c decreases to 572 K at x = 3.03 from 685 K at x = 0. The experimental T_C is lower than the calculated one over the entire range of carbon content. This discrepancy is attributed to the existence of a large amount of nonmagnetic cubic β-Mn and trigonal γ_2-Al_8Mn_5 phases in the experimental samples [3,18]. However, the T_C of 590 K at x = 2.33 is still higher than the 473 K (200 °C), which is the motor operation temperature desired for an EV. Therefore, the x = 2.33 composition is reasonably good for the high magnetization and magnetocrystalline anisotropy.

From the practical application aspect, a permanent magnet motor must withstand elevated temperatures, such as 473 K (200 °C). Therefore, we studied the thermal variation of magnetization σ_s(T) and the magnetocrystalline anisotropy constant K_u(T) for $(Mn_{0.5}Al_{0.5})_{100-x}C_x$ (x = 0 – 3.03) using Eqs. (1)–(4). This is because the saturation magnetization and magnetocrystalline anisotropy constant, i.e., coercivity, determine the maximum magnetic energy product $(BH)_{max} = (B_r - H_c)H_c$ of a magnet. Fig. 8(a) and (b) show the calculated σ_s(T) and K_u(T) as a function of carbon content, respectively. The σ_s (300 K) and K_u (300 K) decrease with increasing the carbon content, but $K_u(0)$ increases, as presented in Table 2. This

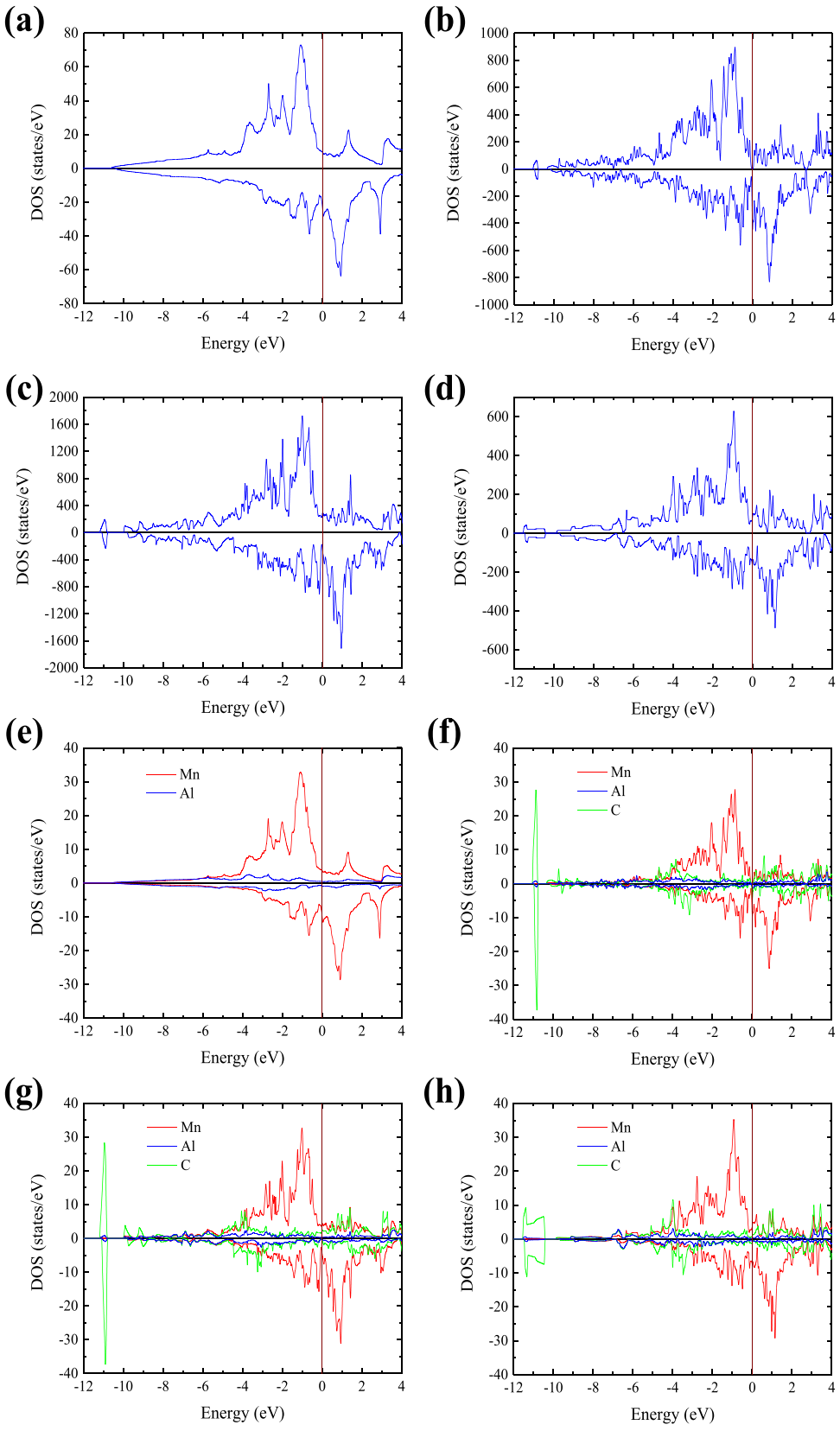

Fig. 6. DOS for $(Mn_{0.5}Al_{0.5})_{100-x}C_x$; (a) x = 0, (b) x = 1.53, (c) x = 2.33, (d) x = 3.03, (e) Partial spin-polarized DOS (pDOS) for x = 0, (f) pDOS for x = 1.54, (g) pDOS for x = 2.33, and (h) pDOS for x = 3.03.

increase is attributed to an increase in the c/a ratio with the carbon (Table 1), while the decrease in K_u(300 K) is because of a decrease in T_C, as shown in Fig. 7. As summarized in Table 3, the magnetization at x = 2.33 is approximately 130 emu/g at 300 K, and the magneto-crystalline anisotropy is 1.02 MJ/m^3. The corresponding $(BH)_{max}$ is 18 MGOe, under $B_s = B_r$ and $H_{ci} > B_r/2$. The theoretical magnetization is

Table 2
Calculated magnetic properties for $(Mn_{0.5}Al_{0.5})_{100-x}C_x$ at 0 K.

x (*at*%)	σ_s (emu/g)	K_u (MJ/m^3)
0	143.47	1.37
0.78	142.53	1.38
1.54	140.85	1.40
2.33	138.49	1.42
3.03	136.73	1.45

Table 3
Curie temperature (T_c), saturation magnetization (σ_s), magneto-crystalline anisotropy constant (K_u) for $(Mn_{0.5}Al_{0.5})_{100-x}C_x$ at 300 K.

x (*at*%)	T_c (K)	σ_s (emu/g)	K_u (MJ/m^3)
0	685	137.96	1.11
0.78	642	135.50	1.07
1.54	614	132.64	1.05
2.33	590	129.14	1.02
3.03	572	126.42	1.01

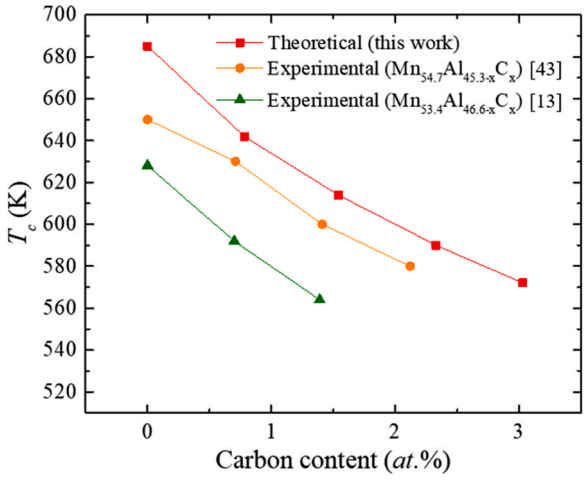

Fig. 7. Curie temperature (T_c) with carbon content.

larger than the experimental magnetization of 116 emu/g for $Mn_{55}Al_{45}$ [44]. Tong et al. reported a saturation magnetization of 125 emu/g for $Mn_{54}Al_{46}$ [45], close to the theoretical value of 138 emu/g at 300 K in this study. Therefore, there is still plenty of

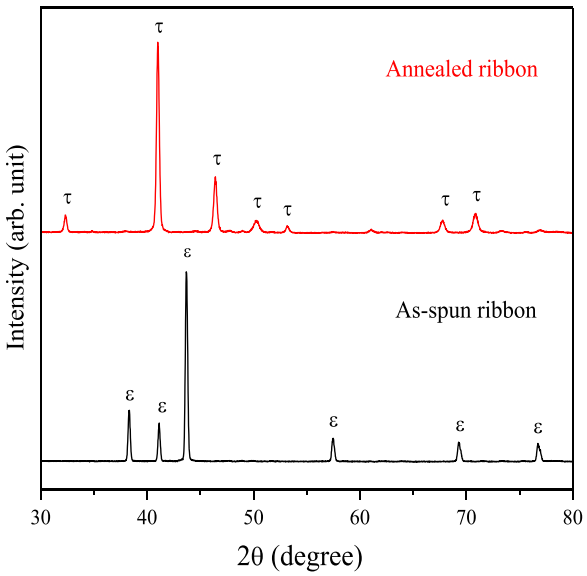

Fig. 9. X-ray diffraction of $(Mn_{0.5}Al_{0.5})_{100-x}C_x$ at x = 2.33.

room for improving the magnetic properties of an $L1_0$ τ-phase Mn-Al magnet for a high $(BH)_{max}$.

Experimental magnetic properties are as follows. The prolonged annealing of τ-phase Mn-Al leads to the decomposition of the τ-phase Mn-Al phase to the equilibrium, paramagnetic β-Mn, and γ_2-Al_8Mn_5 phases [3]. Adding a small amount of C to τ-phase MnAl hinders the decomposition of the τ-phase, thereby increasing saturation magnetization [16]. Further, our theoretical phase stability results in Fig. 5 demonstrate that the τ-phase MnAl is mostly stable at x = 2.33. Accordingly, we have synthesized $(Mn_{0.5}Al_{0.5})_{100-x}C_x$ (x = 0 –3.03) by the preparation method described in Sections 2-2. The synthesized ribbons and powdered samples were characterized to obtain their physical and magnetic properties, using the methods presented in Sections 2-2, to compare with the theoretical results. Fig. 9 shows the XRD patterns of the as-spun and annealed ribbons (x = 2.33). After the annealing of the as-spun sample at 550 °C for 60 min in vacuum and subsequent furnace cooling, the paramagnetic ε-phase (A3 *hcp* structure) of the Mn-Al ribbon transforms to the ferromagnetic τ-phase ($L1_0$ structure) via the B19 orthorhombic structure (ε' phase), as shown in Fig. 2. From an application aspect, we milled annealed ribbons (x = 0.0–3.88) into particles of various sizes, ranging from 25 to 53 μm, which is 30 times larger than the

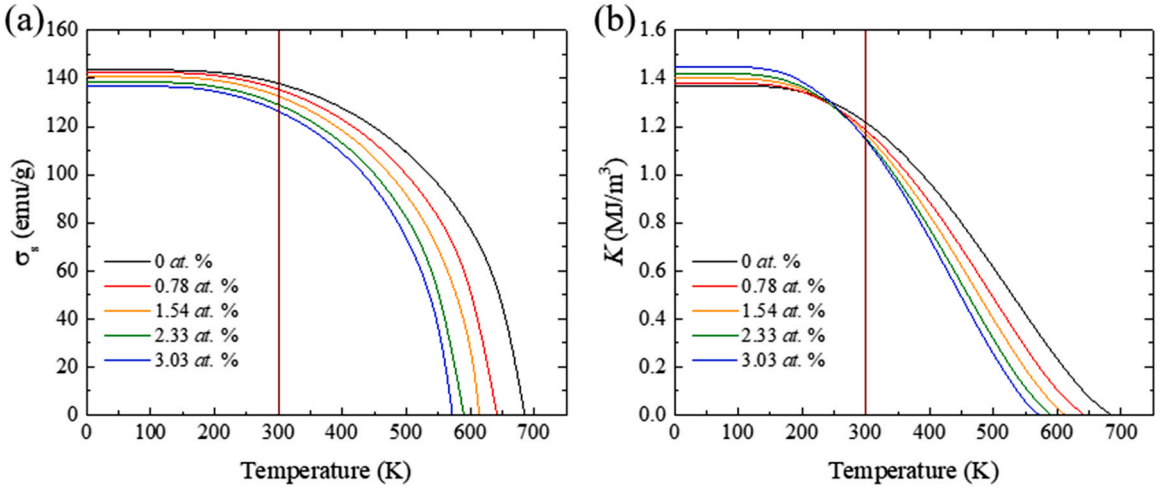

Fig. 8. Temperature dependence of magnetic properties for $(Mn_{0.5}Al_{0.5})_{100-x}C_x$: (a) σ_s(T) and (b) K_u(T).

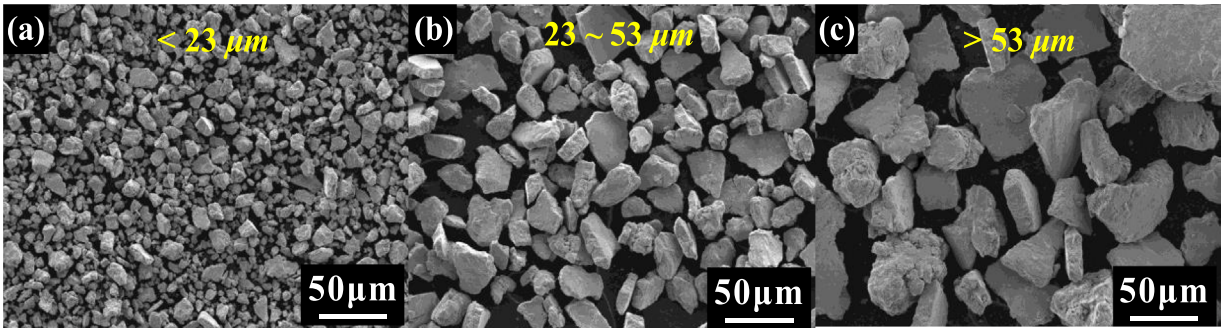

Fig. 10. SEM images after milling and annealing (x = 2.33).

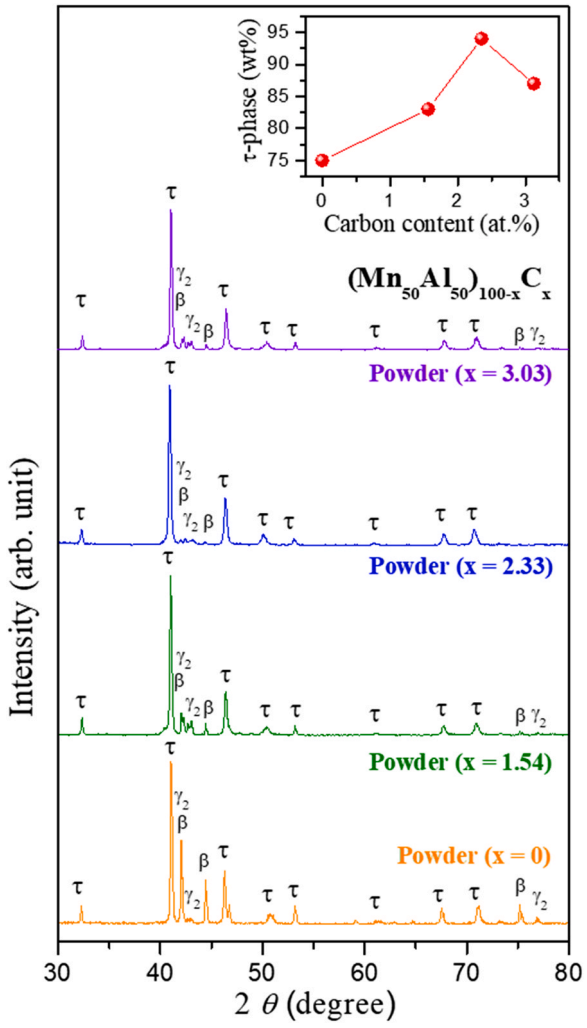

Fig. 11. X-ray diffraction for powders with various carbon contents after milling and annealing. (Inset: weight fraction of the τ-phase in the $Mn_{50}Al_{50-x}C_x$ powder estimated by the Rietveld refinement method using the XRD data).

single magnetic domain size (0.773 μm) of MnAl-C [46]. Scanning electron micrographs of the milled and sieved $(Mn_{0.5}Al_{0.5})_{100-x}C_x$ ($x = 2.33$) particles are shown in Fig. 10.

The phases of the resultant $Mn_{50}Al_{50-x}C_x$ powders with various carbon contents ($x = 0$, 1.54, 2.33, and 3.03) were analyzed by XRD. Fig. 11 presents the XRD data for the powders with particle sizes greater than 53 μm. As shown, non-ferromagnetic equilibrium phases of β and γ_2 are observed in the $Mn_{50}Al_{50-x}C_x$ alloys after grinding into a powder. This indicates that the milling energy by ball milling causes the phase decomposition from the metastable τ-phase to the corresponding stable β- and γ_2-phases despite the short milling time. According to the XRD results, the amounts of β and γ_2 phases in the $(Mn_{0.5}Al_{0.5})_{100-x}C_x$ powders vary depending on the carbon content. The weight fraction of the τ-phase was estimated by the Rietveld refinement method, using the XRD data. As shown in the inset of Fig. 11, the weight fraction of the τ-phase in the $(Mn_{0.5}Al_{0.5})_{100-x}C_x$ powders was found to be 75 wt% at $x = 0$, 83 wt% at $x = 1.54$, 94 wt% at $x = 2.33$, and 87 wt% at $x = 3.03$. The XRD patterns demonstrate that the largest amount of the τ-phase is observed for $(Mn_{0.5}Al_{0.5})_{100-x}C_x$ (x = 2.33; $Mn_{48.835}Al_{48.835}C_{2.33}$), thereby confirming the higher stability of the τ-phase than that of the other compositions. In terms of the magnetic performance, the purity of the τ-phase is the key factor for improving the saturation and remanence magnetizations, because it is the only ferromagnetic phase in the Mn-Al-C system. Therefore, it can be inferred that the σ_s and σ_r values can change according to the fraction of the τ-phase. The results of magnetization shown in Fig. 6 are in good agreement with the trend of the amount of τ-phase observed by XRD analyses. This stability is also in good agreement with the theoretical and experimental magnetization results. Accordingly, the phase stability data shown in Fig. 5 are valid.

Fig. 12 shows the magnetic hysteresis loop for the two representative compositions (x = 0.0, 2.33). All powders (x = 0.0–3.03) were also characterized by VSM for magnetic hysteresis loops; however, only two representative loops are shown. We plotted the carbon content (x) dependence of magnetization and coercivity at 300 K from the measured magnetic hysteresis loops in Fig. 13. Regardless of the particle size, the highest magnetization and coercivity appeared at x = 2.33, mostly stabilizing the τ-phase of Mn-Al. The coercivity increased up to x = 2.33 for all particle sizes and decreased as the carbon content further increased. These results are in good agreement with our theoretically identified carbon content of 2.33 at%.

In summary, even though the present experimental magnetization of approximately 97 emu/g is smaller than the theoretical 130 emu/g at 300 K in Table 3, our calculated lowest formation energy demonstrates that the highest magnetization can be obtained at x = 2.33. This result is in good agreement with previously reported data. This is the first study to calculate the phase stability of τ-phase Mn-Al-C to the best of our knowledge. In this study, we quantify and freshly interpret the reason for the wide reporting of the carbon content of approximately 2 at% for the Mn-Al-C system. The identified carbon content (x = 2.33) sheds light on further improvement of the magnetic properties of the τ-phase Mn-Al-C permanent magnet if the synthetic process is optimized. Considering Mn > 50 at% in Mn-Al, a more stable τ-phase Mn-Al than the Mn-Al with 50 at% Mn can be achieved. Accordingly, it is expected that the τ-phase Mn-Al-C potentially fills the gap between 10 and 30 MGOe magnets. However, a simultaneous enhancement of remanent magnetization and coercivity in the Mn-Al-C system is challenging.

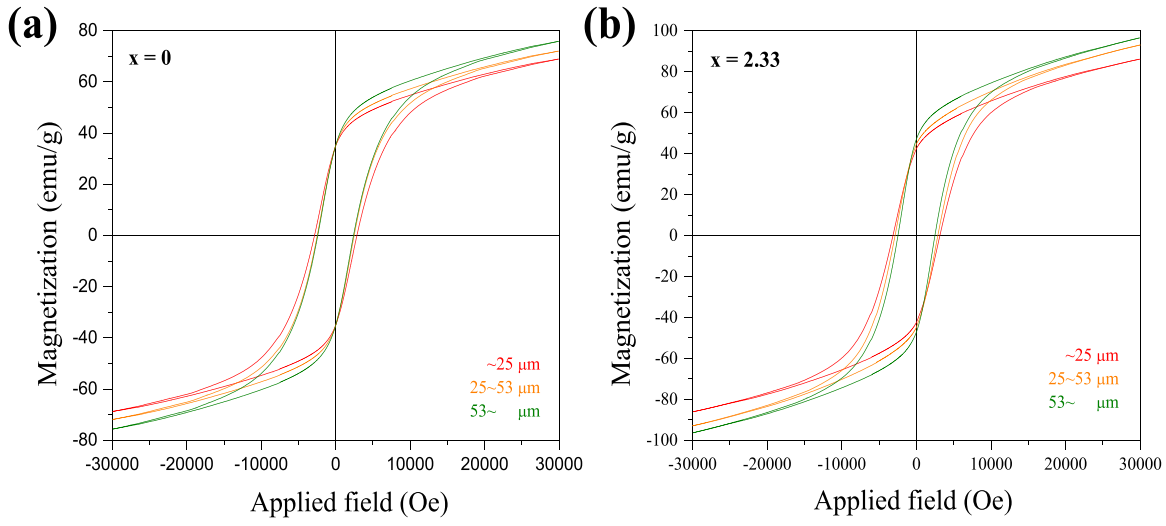

Fig. 12. Magnetic hysteresis loops for milled and annealed $(Mn_{0.5}Al_{0.5})_{100-x}C_x$ powders at room temperature.

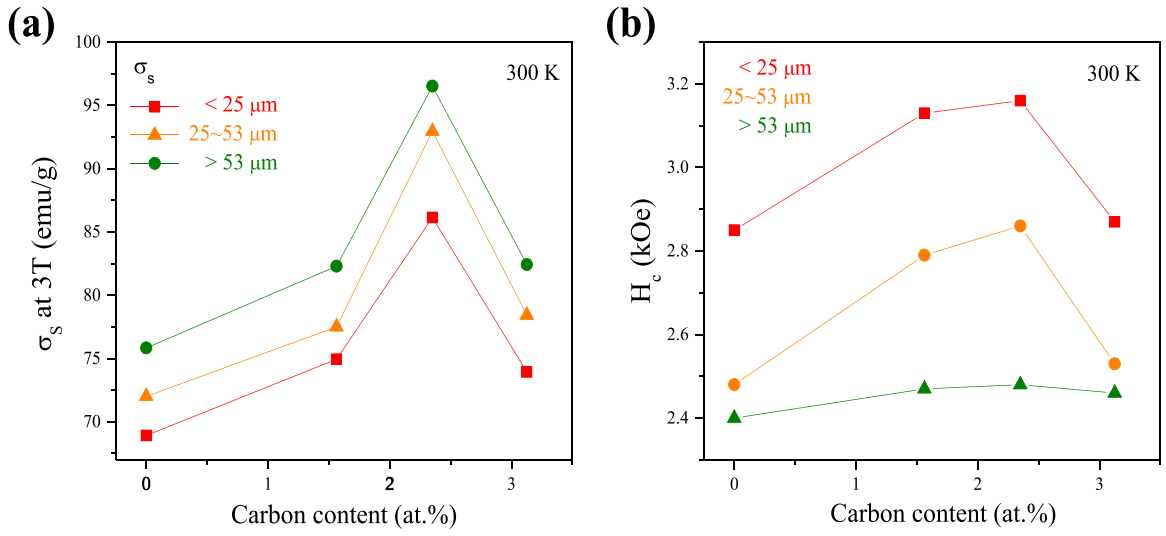

Fig. 13. Carbon content dependence of (a) magnetization at 3 T (σ_{s3T}) and (b) coercivity (H_c) of the milled and annealed $(Mn_{0.5}Al_{0.5})_{100-x}C_x$ (x = 2.33) powdered with various particle sizes.

4. Conclusions

The $Mn_{48.835}Al_{48.835}C_{2.33}$ composition gives the most stable τ-phase of the L_{10}-structured Mn-Al-C. The critical carbon content was confirmed by phase stability calculations and experimental magnetization values. The calculated saturation magnetization and magnetocrystalline anisotropy are approximately 130 emu/g and 1.02 kJ/m^3 at 300 K, respectively. The corresponding $(BH)_{max}$ is 18 MGOe, which is higher than the reported value of 14 MGOe [10,11], but in good agreement with 16.8 MGOe [12]. The estimated Curie temperature is 685 K for $Mn_{50}Al_{50}$ and 590 K for $Mn_{48.835}Al_{48.835}C_{2.33}$. The Curie temperature of 590 K for $Mn_{48.835}Al_{48.835}C_{2.33}$ is still higher than the motor-operating temperature of 473 K. The magnetocrystalline anisotropy constant decreases with increasing carbon content at 300 K, but increases at 0 K. Our calculations predict the magnetic properties of the studied $(Mn_{0.5}Al_{0.5})_{100-x}C_x$ system and are sufficiently fast to estimate the magnetic properties at 300 K, as demonstrated by the experimental results. The results obtained from this study may accelerate the optimization of the synthesis routes for the high-$(BH)_{max}$ Mn-Al-C permanent magnets to fill the gap between 10 and 30 MGOe.

CRediT authorship contribution statement

Sumin Kim: Conceptualization, Investigation, Visualization, Writing – original draft. **Minyeong Choi:** Conceptualization, Methodology, Formal analysis, Writing – original draft. **Hoyun Won:** Methodology, Formal analysis, Visualization. **Hyun-Sook Lee:** Conceptualization, Visualization, Writing – original draft, Writing – review & editing. **Wonchel Lee:** Validation, Visualization. **Seong-Gon Kim:** Validation, Visualization. **Wooyoung Lee:** Conceptualization, Supervision. **Yang-Ki Hong:** Conceptualization, Supervision, Writing – original draft, Writing – review & editing.

Declaration of Competing Interest

The authors declare that they have no known competing financial interests or personal relationships that could have appeared to influence the work reported in this paper.

Acknowledgements

This study was supported by the National R&D Program (NRF-2020M3H4A2084420), the Technology Innovation Program (MOTIE-20013621, Center for Super Critical Material Industrial Technology), and the Priority Research Centers Program (NRF-2019R1A6A1A11055660). Here, NRF is the National Research Foundation of Korea (NRF) funded by the Ministry of Science and ICT in Republic of Korea and MOTIE is the Ministry of Trade, Industry & Energy in Republic of Korea. This study was also supported by the US National Science Foundation Civil, Mechanical, and Manufacturing Innovation Division (NSF-CMMI) under award number 1463301, United States (MYC, HYW, WCL, YKH). H.-S. Lee acknowledges support from the Basic Research in Science and Engineering Program (NRF-2021R1A2C1013690), Republic of Korea.

References

[1] J.M.D. Coey, Permanent magnets: plugging the gap, Scr. Mater. 67 (2012) 524–529.
[2] J. Park, Y.-K. Hong, J. Lee, W. Lee, S.-G. Kim, C.-J. Choi, Electronic structure and maximum energy product of MnBi, Metal 4 (2014) 455–464.
[3] H. Kono, On the ferromagnetic phase in manganese-aluminum system, J. Phys. Soc. Jpn. 13 (1958) 1444–1451.
[4] A.J.J. Koch, P. Hokkeling, M.G.v.d. Steeg, K.J. de Vos, New material for permanent magnets on a base of Mn and Al, J. Appl. Phys. 31 (1960) 75.
[5] H.Y. Yamamoto, Magnet Alloys, U.S. Patent 3 661567, 1972.
[6] J.H. Park, Y.K. Hong, S. Bae, J.J. Lee, J. Jalli, G. Abo, N. Neveu, S.G. Kim, C.J. Choi, J.G. Lee, Saturation magnetization and crystalline anisotropy calculations for MnAl permanent magnet, J. Appl. Phys. 107 (2010) 09A731.
[7] A. Sakuma, Electronic structure and magnetocrystalline anisotropy energy of MnAl, J. Phys. Soc. Jpn. 63 (1994) 1422–1428.
[8] W. Zhang, B. Balasubramanian, P. Kharel, R. Pahari, S.R. Valloppilly, X. Li, L. Yue, R. Skomski, D.J. Sellmyer, High energy product of MnBi by field annealing and Sn alloying, APL Mater. 7 (2019) 121111.
[9] J.H. Park, Y.K. Hong, S.G. Kim, S.H. Kim, L.S.I. Liyanage, J.J. Lee, W.C. Lee, G.S. Abo, K.H. Hur, S.Y. An, Maximum energy product at elevated temperatures for hexagonal strontium ferrite (SrFe12O19) magnet, J. Magn. Magn. Mater. 355 (2014) 1–6.
[10] J.M.D. Coey, Hard magnetic materials: a perspective, IEEE Trans. Magn. 47 (2011) 4671–4681.
[11] J.M.D. Coey, Magnetism and Magnetic Materials, Cambridge University Press, 2010.
[12] J. Cui, M. Kramer, L. Zhou, F. Liu, A. Gabay, G. Hadjipanayis, B. Balasubramanian, D. Sellmyer, Current progress and future challenges in rare-earth-free permanent magnets, Acta Mater. 158 (2018) 118–137.
[13] T. Ohtani, N. Kato, K. Kojima, Y. Sakamoto, I. Konno, M. Tsukahara, T. Kubo, Magnetic properties of Mn-Al-C permanent magnet alloys, IEEE Trans. Magn. 13 (1977) 1328–1330.
[14] J. Van Den Broek, H. Donkersloot, G. Van Tendeloo, J. Van, Landuyt, Phase transformations in pure and carbon-doped $Al_{45}Mn_{55}$ alloys, Acta Met. 27 (1979) 1497–1504.
[15] C. Yanar, J. Wiezorek, W. Soffa, V. Radmilovic, Massive transformation and the formation of the ferromagnetic L10 phase in manganese-aluminum-based alloys, Metall. Mater. Trans. A 33 (2002) 2413–2423.
[16] X. Tong, P. Sharma, A. Makino, Investigations on low energy product of MnAl magnets through recoil curves, J. Phys. D: Appl. Phys. 53 (2020) 175001.
[17] Z. Xianga, X. Wanga, Y. Songa, L. Yub, E. Cuib, B. Denga, D. Bataluc, W. Lua, Effect of cooling rates on the microstructure and magnetic properties ofMnAl permanent magnetic alloys, J. Magn. Magn. Mater. 475 (2019) 479–483.
[18] H. Fang, J. Cedervall, F.J.M. Casado, Z. Matej, J. Bednarcik, J. Ångström, P. Berastegui, M. Sahlberg, Insights into formation and stability of-MnAlZ_x (Z = C and B), J. Alloy. Compd. 692 (2017) 198–203.
[19] P. Müller, B.E. Bürgler, H. Heinrich, A.S. Sologubenko, G. Kostorz, Observation of the shear mode of the $\varepsilon \rightarrow \tau$ phase transformation in a Mn-Al-C single crystal, Philos. Mag. Lett. 82 (2002) 71–79.
[20] V.T. Nguyen, F. Calvayrac, A. Bajorek, N. Randrianantoandro, Mechanical alloying and theoretical studies of MnAl(C) magnets, J. Magn. Magn. Mater. 462 (2018) 96–104.
[21] H. Fang, S. Kontos, J. Ångström, J. Cedervall, P. Svedlindh, K. Gunnarsson, M. Sahlberg, Directly obtained τ-phase MnAl, a high performance magnetic material for permanent magnets, J. Solid State Chem. 237 (2016) 300–306.
[22] M.V. Gorshenkov, D.Y. Karpenkov, R.V. Sundeev, V.V. CheverikinI, V. Shchetinin, Mater. Lett. 272 (2020) 1278.
[23] A. Pasko, F. Mazaleyrat, M. LoBue, E. Fazakas, L.K. Varga, Hard magnetic properties of melt-spun Mn-Al-C alloys, EPJ Web Conf. 40 (2013) 06008.
[24] P. Nieves, S. Arapan, T. Schrefl, S. Cuesta-Lopez, Atomistic spin dynamics simulations of the MnAl τ-phase and its antiphase boundary, Phys. Rev. B 96 (2017) 224411.
[25] P.C. Kuo, Y.D. Yao, W.R. Chen, J.H. Huang, Preparation and magnetical studies of $Mn_{50}Al_{50}$/Al bilayer films, J. Appl. Phys. 81 (1997) 5253.
[26] J.P. Perdew, K. Burke, M. Ernzerhof, Generalized gradient approximation made simple, Phys. Rev. Lett. 77 (1996) 3865–3868.
[27] G. Kresse, J. Hafner, Ab initio molecular dynamics for liquid metals, Phys. Rev. B 47 (1993) 558–561.
[28] G. Kresse, J. Furthmüller, Efficient iterative schemes for ab initio total-energy calculations using a plane-wave basis set, Phys. Rev. B 54 (1996) 11169–11186.
[29] P. Blaha, K. Schwarz, F. Tran, R. Laskowski, G.K.H. Madsen, L.D. Marks, WIEN2k: an APW+lo program for calculating the properties of solids, J. Chem. Phys. 152 (2020) 074101.
[30] M. Chakraborty, J. Spitaler, P. Puschnig, C. Ambrosch-Draxl, ATAT@WIEN2k: an interface for cluster expansion based on the linearized augmented planewave method, Comput. Phys. Commun. 181 (2010) 913–920.
[31] G. Kresse, M. Marsman, J. Furthmüller, VASP the GUIDE, institut für materialphysik, Univ. Wien. 46 (2018).
[32] J.M. MacLaren, T.C. Schulthess, M. McHenry, Electronic structure, exchange interactions, and Curie temperature of FeCo, J. Appl. Phys. 85 (1999) 4833–4835.
[33] A. van de Walle, M. Asta, G. Ceder, The alloy theoretic automated toolkit: a user guide, CALPHAD, Journal 26 (2002) 539–553.
[34] S. Muller, Bulk and surface ordering phenomena in binary metal alloys, J. Phys.: Condens Matter 15 (2003) R1429–R1500.
[35] A. van de Walle, G. Ceder, Automating first-principles phase diagram calculations, J. Phase Equilib. 23 (2002) 348–359.
[36] H.B. Callen, E. Callen, The present status of the temperature dependence of magnetocrystalline anisotropy, and the $l(l+1)2$ power law, J. Phys. Chem. Solids 27 (1966) 1271–1285.
[37] A. Pasko, M. LoBue, E. Fazakas, L.K. Varga, F. Mazaleyrat, Spark plasma sintering of Mn–Al–C hard magnets, J. Phys.: Condens. Matter 26 (2014) 064203.
[38] M.J. Lucis, T.E. Prost, X. Jiang, M. Wang, J.E. Shield, Phase transitions in mechanically milled Mn-Al-C permanent magnets, Metals 4 (2014) 130–140.
[39] Q. Zeng, I. Baker, J.B. Cui, Z.C. Yan, Structural and magnetic properties of nanostructured Mn–Al–C magnetic materials, J. Magn. Magn. Mater. 308 (2007) 214–226.
[40] K.D. Volkov, E.N. Tarasov, A.V. Zinin, Met. effect of the crystallization conditions of alloy Mn54Al43C3 on the magnetic properties of mechanically milled powder, Sci. Heat. Treat. 58 (2017) 599–602.
[41] S. Kim, H. Moon, H. Jung, S.-M. Kim, H.-S. Lee, H. C.-Y, W. Lee, Magnetic properties of large-scaled MnBi bulk magnets, J. Alloy. Compd. 708 (2017) 1245–1249.
[42] K.H. Han, C.T. Lee, W.K. Choo, On the position of carbon atom in the τ-phase of carbon-doped Mn-Al permanent magnets, Phys. Status Solidi A 136 (1993) 21–28.
[43] H. Harada, Hard magnetic materials: Mn-Al-C, ferrites, in: P. Beiss, R. Ruthardt, H. Warlimont (Eds.), Powder Metallurgy Data: Part1 Metals and Magnets, 2A1 Springer-Verlag, Berlin Heidelberg, 2003, pp. 9–79.
[44] D. Palanisamy, G. Madras, K. Chattopadhyay, Exploring the pathways for enhancing the hard magnetic properties of binary Al-55 at%Mn Heusler alloy through mechanical alloying, J. Magn. Magn. Mater. 439 (2017) 181–187.
[45] X. Tong, P. Sharma, A. Makino, Investigations on low energy product of MnAl magnets through recoil curves, J. Phys. D: Appl. Phys. 53 (2020) 175001.
[46] J. Thielsch, F. Bittner, T.G. Woodcock, Magnetization reversal processes in hot-extruded τ-MnAl-C, J. Magn. Magn. Mater. 426 (2017) 25–31.